Available online at www.sciencedirect.com

ScienceDirect

journal homepage: http://www.elsevier.com/locate/acme

Original Research Article

The effect of microstructure anisotropy on low temperature fracture of ultrafine-grained iron

Barbara Romelczyk-Baishya [a,*], *Krzysztof Łęczycki* [a], *Magdalena Płocińska* [a], *Mariusz Kulczyk* [b], *Rafał Molak* [a], *Zbigniew Pakieła* [a]

[a] *Warsaw University of Technology, Faculty of Materials Science and Engineering, 141 Woloska St., 02-507 Warsaw, Poland*

[b] *Institute of High Pressure Physics, Polish Academy of Sciences, 29/37 Sokolowska St., 01-142 Warsaw, Poland*

ARTICLE INFO

Article history:
Received 14 December 2017
Accepted 26 February 2018
Available online 10 April 2018

Keywords:
Iron
Nanomaterial
Fracture
Low temperature
Small punch test

ABSTRACT

This papers deals with the character on low (−180 °C) temperature fracture of iron. Microcrystalline and ultrafine-grained (UFG) iron rods were investigated. To obtain UFG material 20 mm in diameter iron rod was hydrostatically extruded (HE) in two steps: from 20 to 12 mm and from 12 to 8 mm. Because of microstructure anisotropy caused by HE mini-disc and mini-beam samples were cut off from perpendicular and longitudinal cross-section of the rods. Microcrystalline rod fractured in brittle manner at low temperature for both cross-sections, but in UFG iron fracture character depended on grain's shape. For samples were crack propagates parallel to the grain's elongation axis intercrystalline fracture occurred. For mini-beams were crack propagates crosswise to the grain elongation axis transcrystalline fracture occurred and force deflection curve was similar to those obtained for room temperature.

* *Corresponding author.*
E-mail address: barbara.romelczyk@inmat.pw.edu.pl (B. Romelczyk-Baishya).

Abbreviations: DBTT, ductile–brittle transition temperature; UFG, ultrafine-grained material; MC, microcrystalline material; HE, hydrostatic extrusion; SPD, severe plastic deformation; SPT, small punch test; Fe20, iron rod of 20 mm in diameter; HE8, iron rod of 8 mm in diameter obtained via hydrostatic extrusion; HE8F, iron rod of 8 mm in diameter obtained via HE and then flattened.; YS, yield stress; UTS, ultimate tensile stress; RT, room temperature used as the environment for test; −180 °C, temperature used as the environment for low temperature test; F_y, yielding force for SPT; F_u, ultimate (maximum) force for SPT; F_f, fracture force for SPT; U_y, yielding deflection for SPT; U_u, ultimate deflection for SPT; U_f, fracture deflection for SPT; F_y_RT, yielding force at room temperature; F_u_RT, ultimate force at room temperature; F_f_RT, fracture force at room temperature; U_y_RT, yielding deflection at room temperature; U_u_RT, ultimate deflection at room temperature; U_y_RT, fracture deflection at room temperature; F_y_-180 °C, yielding force at −180 °C; F_u_-180 °C, ultimate force at −180 °C; F_f_-180 °C, fracture force at −180 °C; U_y_-180 °C, yielding deflection at −180 °C; U_u_-180 °C, ultimate deflection at −180 °C; U_y_-180 °C, fracture deflection at −180 °C.

https://doi.org/10.1016/j.acme.2018.02.014
1644-9665/

1. Introduction

Metals with a body-centred cubic structure such as iron exhibit a ductile–brittle transition temperature (DBTT) which results in a brittleness threshold below a particular temperature. At low temperatures, dislocation mobility is limited and a crack tip cannot be blunted, which results in a fracture process [1]. For bcc materials it was found that cleavage fracture mainly occurs for the 100 plane. The temperature of brittle fracture depends on deformation velocity [2], the shape and size of the specimens investigated [3] and also on the material's purity [4], grain size [5] and texture [6].

It is known that grain refinement can be an efficient way to shift transit temperature. For example, microcrystalline iron brittle fracture usually occurs below −70 °C [7], while the ultrafine-grained (UFG) counterpart preserves ductile fracture even in liquid nitrogen. Romelczyk et al. have obtained ductile fracture after Charpy impact test for iron sinter deformed via hydrostatic extrusion (HE) [5]. Gizynski et al. observed ductile behaviour for technically pure UFG iron rod while dynamic tensile test [2]. Hohenwarter et al. obtained a higher DBTT for submicrocrystalline grain Armco iron than for the microcrystalline counterparts [8]. The most popular group of methods that leads to obtaining UFG and nanocrystalline-grained (NC) products is severe plastic deformation (SPD). This includes: equal-channel angular pressing (ECAP) [9], high-pressure torsion (HPT) [10], hydrostatic extrusion [11], accumulative roll bonding (ARB) [12], and many others. The main idea of SPD is to generate big amount of new dislocations during the deformation process that result in fine-grained microstructure [13]. In general NC materials have high strength and low ductility due to their high dislocation density. The high density of dislocations quickly reaches saturation, which contributes to an early, localized deformation in the form of necking [14]. Indeed, some experiments show that it is possible to preserve ductility after SPD [15].

The basic criterion of ductile or brittle fracture was proposed by Rice [16], and can be explained as a competition between cleavage and dislocation emission from the crack front. Based on this, Gizynski et al. [2] proposed that to obtain ductile fracture, the dislocation must be closer than a certain critical distance to the crack front. In this case, the dislocation near the crack front is subjected to a slip in the stress field of the crack front. As the stress rapidly decreases with the distance from the crack front, when the dislocation is too far from the front, the stress will be too low to move the dislocation and slip will not occur. In UFG materials the dislocation density can be large enough that the average distance between them is less than the critical and ductile fracture can occur. When the dislocation density is too low, the average distance between them is greater than the critical distance and in such case a cleavage is observed. Gizynski et al. [2] have shown that the iron with dislocation density greater than a critical one breaks in a ductile manner even at impact tensile test in liquid nitrogen. They tested UFG iron produced by hydrostatic extrusion, with grains elongated parallel to the extrusion direction, but only specimens where cracks were propagating perpendicularly to the direction of grain elongation was investigated. In their work, they did not analyze the influence of the cracks propagation path on the behaviour of the material.

According to Ovid'ko's and Sheinerman's [17] theoretical analysis of UFG materials, dislocations emitted from a crack are blocked at grain boundaries as crack blunting. This results in decreasing ductility, but it must be added that this mechanism is not popular in nanomaterials. Armstrong and Antolovich [18] have proposed that the cracking mode depends on a piling up of dislocations. He assumed that cleavage cracking should not occur in the case of small numbers of dislocations in the pile-up at the front edge of the crack.

Hohenvarter and Pippan proved that the crack propagation, path and fracture resistance of a material is strongly dependent on grain orientation. In [6] they reported about iron produced via HPT. Specimens were prepared in such way that three different crack plane orientation were investigated. It was found that fracture toughness value strongly depended of crack propagation path. Similar results were obtained for iron produced via ECAP [19]. Iron produced via HPT was investigated by Leitner [20]. Specimens from four different direction was prepared for fatigue crack propagation test. The

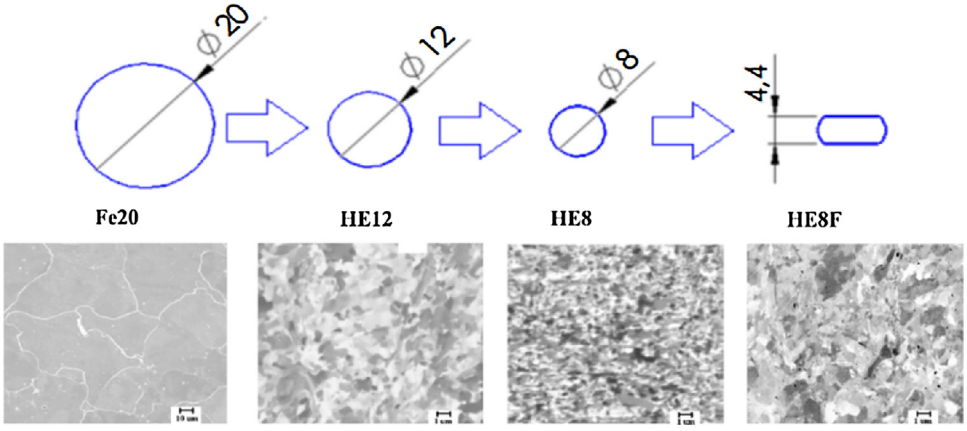

Fig. 1 – The scheme of material processing.

fracture mode was depended on grains orientation and crack propagation path. Research mentioned above was focused on the properties obtained at room temperature.

This research investigates the influence of anisotropy on fracturing for technically pure MC and UFG iron at room temperature and −180 °C. The UFG material was produced via hydrostatic extrusion. The final product was in the form of rods of different diameters. Because of the small diameter of the rods, a small punch test was applied for the mechanical tests. The experiments were carried out on mini-disc and mini-beam specimens.

2. Material and experimental methods

A technically pure iron rod of 20 mm in diameter (denoted as Fe20) was hydrostatically extruded in 2 steps: from 20 to 12 mm and from 12 to 8 mm (denoted as HE8). Then, 8 × 40 mm pieces of rod were flattened using a Zwick/Roell Z250 tensile machine with a crosshead velocity of 0.008 mm/s. This processing step was used to obtain a larger number of specimens from the perpendicular diameter. A force of 240 kN was applied to deform the pieces of rod, and the final product thickness was about 4.4 (denoted as HE8F). A scheme of the process and subsequent microstructures is presented in Fig. 1.

The chemical composition of the material was measured using an optical emission spectrometer Meteorex ARC-MET 930. The microstructure of the Fe20 was revealed using an Electron Scanning Microscope Hitachi SU-3500 microscope. Polished Fe20 iron specimens were etched by means of Nital 4% (4% HNO_3 + 96% C_2H_5OH) for 15 s. The microstructure of the HE8 and HE8F were examined using a Hitachi SU-8000 Electron Scanning Microscope on tunnelling channel mode. Polished specimens were ionic etched before microscopic observations. The process was made by means of Hitachi IM-4000 ion beam milling machine. The transverse cross-section of HE8 was examined by means of transmission Electron Microscopy JOEL JEM 1200 EX II. For Fe20 and HE8 stereological analyses were carried on the registered microstructures using Micro Meter 1.0 software [21].

Table 1 – Description of the specimens.

Shape	Direction	Temperature	Fe20	HE8	HE8F
Mini-disc	L	RT	Fe20_L_RT	–	HE8F_L_RT
		−180 °C	Fe20_L_-180 °C	–	HE8F_L_-180 °C
	T	RT	Fe20_T_RT	HE8_T_RT	–
		−180 °C	Fe20_T_-180 °C	HE8_T_-180 °C	–
Mini-beam	L1	RT	Fe20_L1_RT	–	HE8_L1_RT
		−180 °C	Fe20_L1_-180 °C	–	HE8_L1_-180 °C
	T1	RT	Fe20_T1_RT	–	HE8_T1_RT
		−180 °C	Fe20_T1_-180 °C	–	HE8_T1_-180 °C
	T2	RT	Fe20_T2_RT	–	HE8_T2_RT
		−180 °C	Fe20_T2_-180 °C	–	HE8_T2_-180 °C

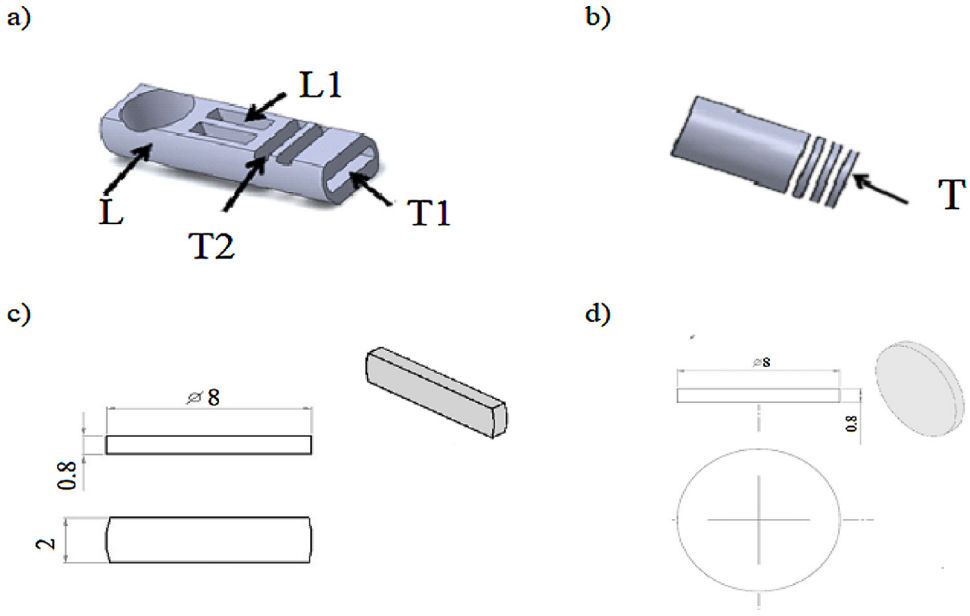

Fig. 2 – Scheme of cutting of specimens: (a) general view of HE8F rod, (b) general view of HE8 and Fe20 rods, (c) draw of mini-beams, (d) draw of mini-disc.

Vickers microhardness tests were carried out using a Zwick/Roell ZHU 0.2 hardness tester. Microhardness was measured under a load of 0.2 kg applied for 15 s on the polished specimens across the transverse cross-section. The distance between single measurements for Fe was 1 mm and for HE8 and HE8F was 0.5 mm.

Uniaxial tensile tests were carried out at room temperature using a Zwick 005 universal testing machine. Tensile tests were conducted under the displacement control mode at an initial strain rate of 10^{-3} 1/s. Mini-samples of an 8.6 mm total length, 5 mm gauge section length and 0.5 × 0.8 cross-section were used for those tests. Three specimens were measured for each material. For the Fe20, the mini-samples were cut off from the longitudinal and transverse cross-sections. For the HE8, the mini-samples were prepared from the longitudinal direction only. It was due to too small dimension in transverse cross-section of HE8. The strain was measured using Digital Image Correlation (DIC) software. Images were recorded at 4 fps and then post-processed [22]. Based on the load displacement data, the yield stress (YS) and ultimate tensile stress (UTS) were estimated.

For the influence of microstructure anisotropy on the mechanical properties of the iron, the Small Punch Technique (SPT) was employed. SPT is a method that requires only a small volume of material. The method was originally designed for the nuclear industry [23], but then spread to other areas. It is now widely used to estimate such properties as yield and ultimate stress [24], DBTT [25], creep strength [26], and fracture toughness [27]. Furthermore, the shape of SPT specimens can be useful when examining anisotropic materials [28].

The tests were carried out using a Zwick/Roell Z005 universal testing machine equipped with a 5 kN load cell. The crosshead velocity was 2 mm/min for each test. For the deflection measurements, an electromechanical extensometer MTS 634-12F-25 was used. Because of the limitations of the puncher length, specimens having a deflection of more than 2 mm were not registered. The experiments were conducted at room temperature (denoted as RT) and at −180 °C (denoted as -180 °C).

Two kinds of specimens were prepared for testing: mini-discs and mini-beams. All of the specimens were cut off by electrical discharge machining (EDM), with an addition of 0.3 mm in thickness. The specimens were then ground on abrasive papers to remove the recast layer created during EDM [29]. The final surface was prepared using #2400 paper. The final dimensions of the discs were 8 mm in diameter and 0.8 mm in thickness. The specimens were cut in the longitudinal (“L”) and transverse (“T”) directions. The disc

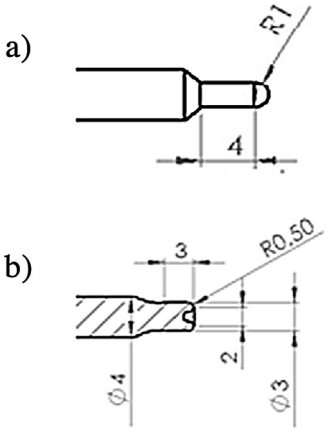

Fig. 3 – Shape of puncher (a) spherical, (b) tubular.

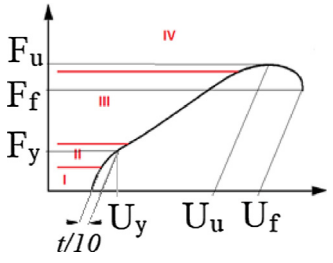

Fig. 5 – Force–deflection curve obtained from SPT.

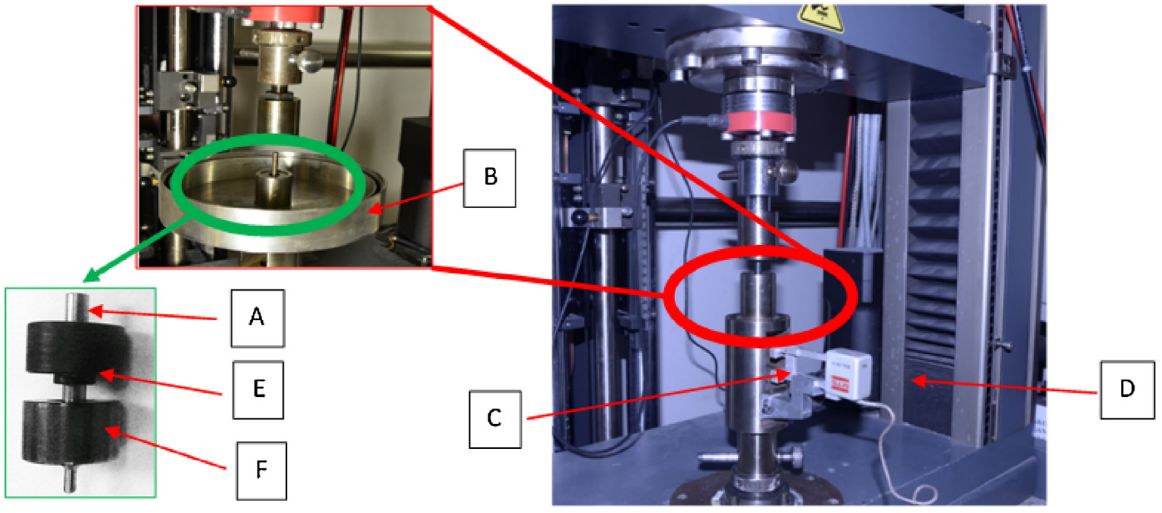

Fig. 4 – Stand used for SPT: (a) puncher, (b) LN chamber, (c) sleeve, (d) extensometer, (e) clamping die, (f) receiving die.

Table 2 – Chemical composition of iron rod.

Component	Fe	C	Cr	Mn	Cu	Ni	P	S	Si	Al
Mass %	Balance (99.62)	0.023	0.089	0.068	0.038	0.026	0.015	0.014	0.006	0.002
St dev.		0.006	0.001	0.051	0.001	0.001	0.003	0.000	0.000	0.003

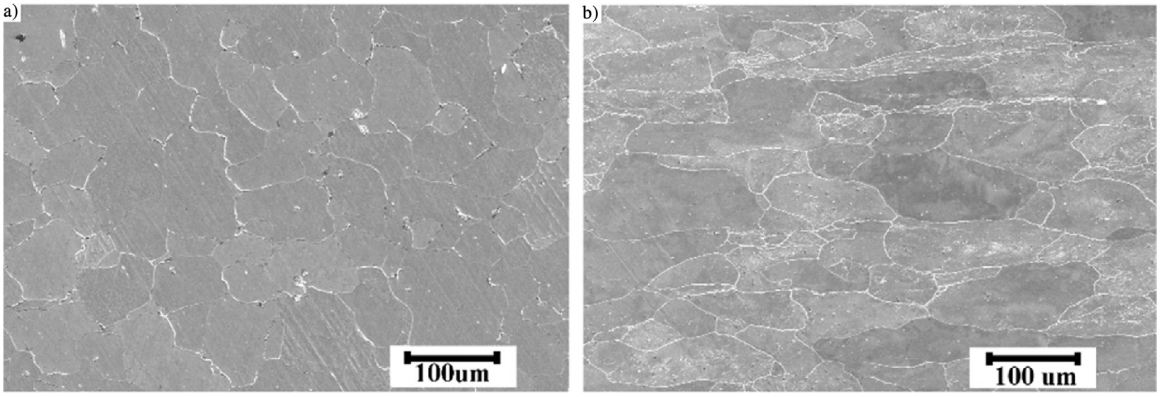

Fig. 6 – Microstructure of Fe20 (a) transverse, (b) longitudinal cross-section.

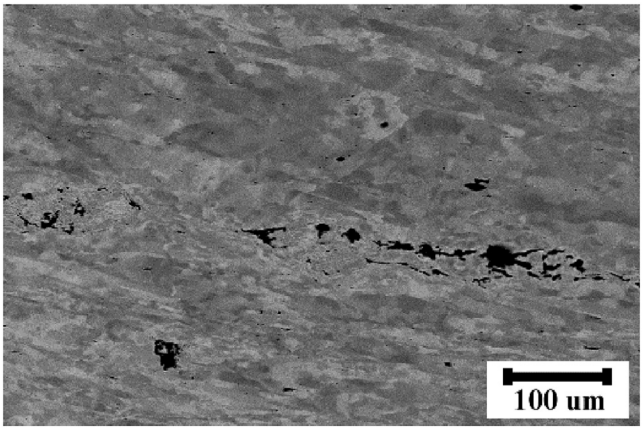

Fig. 7 – Discontinuity at longitudinal cross-section revealed in iron rod via SEM observation.

specimens were prepared from the Fe20 rod (denoted as ''Fe20_L'' and ''Fe20_T''). The HE8_T specimens were cut off from the HE8 material. The HE8_L specimens were prepared from the HE8F rod.

Table 1 shows the description of the mini-disc and mini-beam specimens prepared for this investigation. For each material's conditions 3–7 mini-disc and mini-beam were investigated.

To control crack propagation and then make it is easier to identify the influence of anisotropy on the mechanical properties, the mini-beam specimens were designed. They were 0.8 mm in thickness, 2 mm in width, and 8 mm in length. They were cut from the HE8F and Fe20 rods in three mutually perpendicular directions (Fig. 2).

For the disc specimens, a spherical puncher of 1 mm radius (Fig. 3a) was used, while for mini-beams a tubular-shaped puncher with an outer diameter of 3 mm and an inner diameter of 2 mm was employed (Fig. 3b). The tubular puncher ensured a symmetrical loading of the width of the specimens.

The specimens were mounted between a clamping and a receiving die and then fixed by means of a nut. The nut was screwed to a sleeve, with 15 N m of torque for the discs. To obtain a similar clamping force, 5 N m of torque was used for beams. The diameter of the receiving die was 5.4 mm. Under the specimens, the extensometer was mounted. The SPT stand used for investigation is shown in Fig. 4.

Force–deflection curves were registered during the SPT. An exemplary force–displacement curve with its characteristic parameters estimated during the SPT and the 4 zones typical of ductile materials is presented in Fig. 5: (I) elastic bending, (II) elastoplastic transition, (III) membrane stretching/general plastic deformation, and (IV) plastic instability [30]. The yielding force (F_y) was estimated as the initial slope shifted by $t/10$ where ''t'' is the initial thickness of the specimen. The ultimate force (F_u) is the maximum force registered during the test. The failure force (F_f) is the force when the load applied is less than $0.8F_u$. U_y, U_u and U_f are corresponding deflections.

3. Results and discussion

Table 2 shows the chemical composition of the iron rod investigated.

The microstructure of the Fe20 is shown in Fig. 6. The average grain size was estimated as $55 \pm 26\ \mu m$ in the transverse cross-section and $72 \pm 42\ \mu m$ in the longitudinal cross-section.

In the microstructure, cracks were present oriented along the longitudinal cross-section. A photo of the specimen's cracks is shown in Fig. 7.

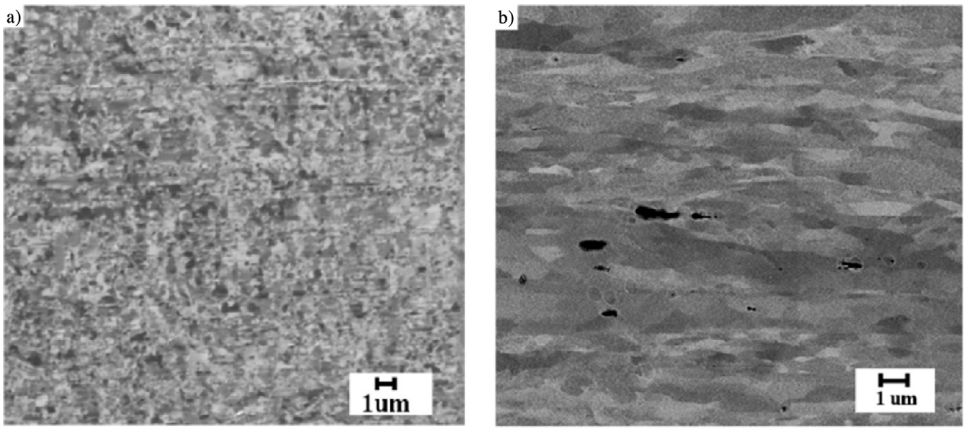

Fig. 8 – HE8 microstructure of (a) transverse, (b) longitudinal cross-section.

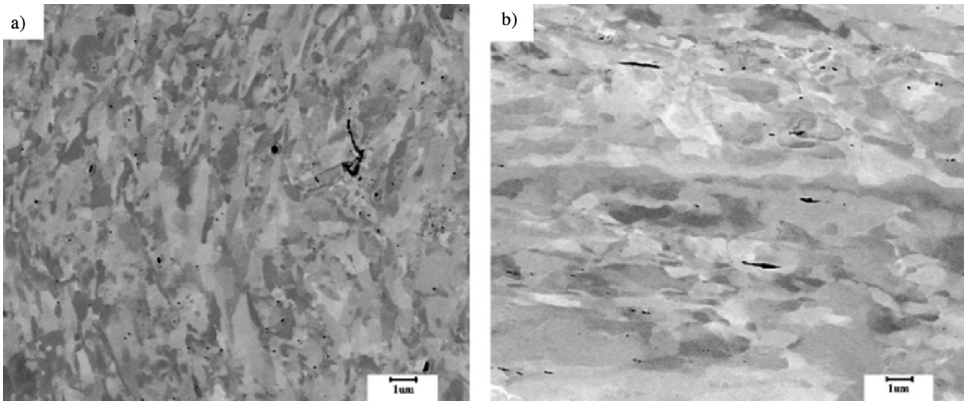

Fig. 9 – HE8F microstructure of (a) transverse, (b) longitudinal cross-section.

In the longitudinal cross-section of the HE8 iron (Figs. 7 and 8b) and HE8F (Fig. 9b), elongated grains were revealed. In the transverse cross-section, equiaxial grain shapes were present. In the transverse cross-section, the structure was finer than in longitudinal cross-section. The average grain size measured in the transverse cross-section of the HE8 was estimated as 260 $\pm$ 125 nm. Detailed microstructure analyses, which were carried out by means of transmission electron microscopy and the EBSD technique, were presented in a previous investigation carried out on this material by Gizynski et al. [2].

The results of the microhardness measurements are shown in Fig. 10 and Table 3.

The value of standard deviation for all specimens was less than 5%. For Fe20 and HE8F the difference between min and max values was about 40, but for HE8 was 80. This was caused by discontinuity in the material mention above (Fig. 7).

Hydrostatic extrusion caused a significant increase in the HV0.2 value, from 141 for the Fe20 to 228 for the HE8. The total strain of HE8 was 1.83 compared with Fe20, this caused strain hardening of material and resulted in almost double increase in microhardness. Flattening the HE8 rod caused no further increase in the average hardness value.

Stress–strain curves for tensile tests are presented in Fig. 11. The results obtained from the mini-sample tensile tests are presented in Table 4.

The UFG specimens exhibit a higher yield, higher ultimate tensile stress, and lower elongation to failure than the MC iron. Grains refinement during hydrostatic extrusion result in increase in strength of HE8 and decrease in ductility. Fine-grained metals exhibit higher strain localization, which results in a decrease in plasticity [31].

3.1. *Small punch test – disc specimens*

The exemplary force–deflection curves are shown in Fig. 12. The average values of yield, ultimate and failure force for different materials and temperatures obtained for the disc specimens are shown in Fig. 13. The average deflections (yield, ultimate and failure) for those specimens are presented in Fig. 14.

All of the discs tested at room temperature show behaviours typical of ductile materials, in the force–deflection curves 4 zones were observed for each specimen (Fig. 12).

All discs tested at room temperature showed behaviour typical of ductile materials. In the force–deflection curves, 4 zones were observed for each specimen. At RT, UFG iron shows higher strength than MC. This was expected based on Hall–Patch relation which proves that mechanical properties are inversely proportional to the grain size. Both the micro- and ultrafine-grained iron had a similar force value for the

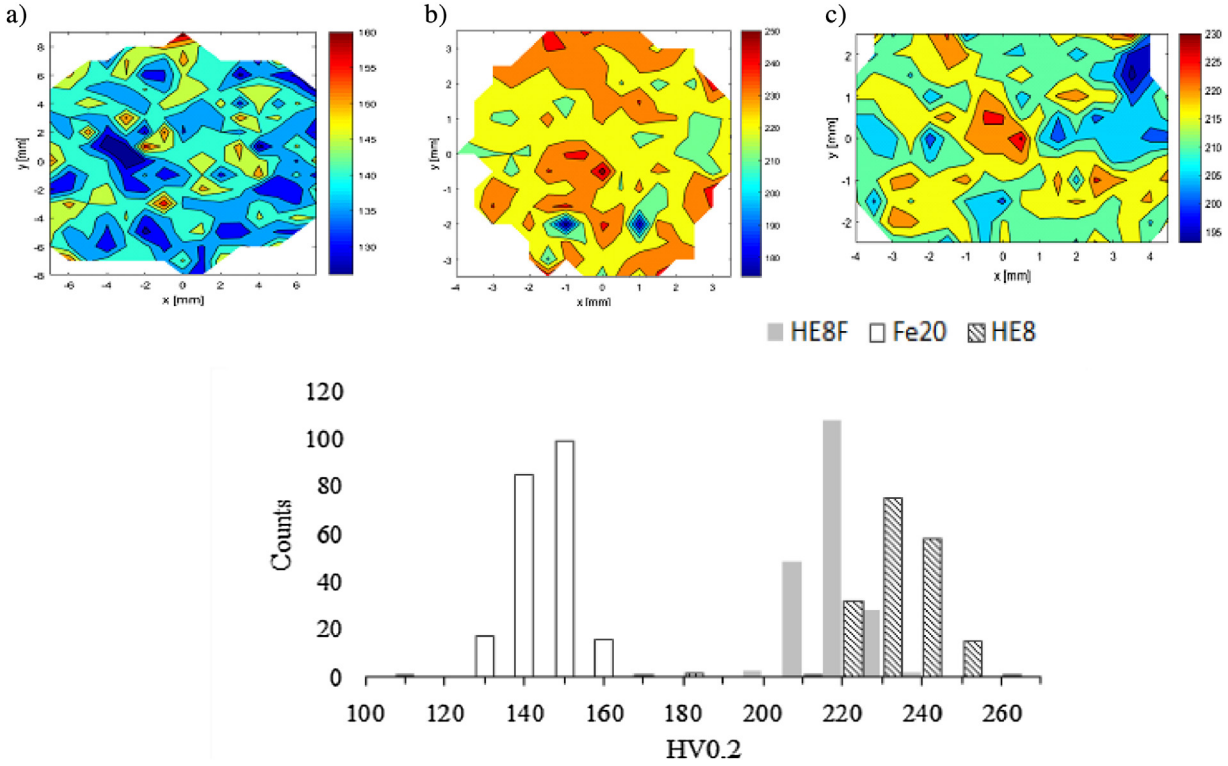

Fig. 10 – Microhardness maps and histograms of iron rods: (a) Fe20, (b) HE8, (c) HE8F.

Table 3 – The results of microhardness obtained for transverse cross-section of rods.

HV0.2	Fe20	HE8	HE8F
Average	141	228	214
SD	7	10	6
Min	110	174	193
Max	164	256	231
Median	141	227	214
Number of measurements	218	184	190

Table 4 – Tensile test results with standard deviation measured for mini-samples (L – longitudinal direction, T – transverse direction).

	YS [MPa]	UTS [MPa]	A [%]
Fe20_T	290 ± 6	295 ± 3	19.9 ± 2.0
Fe20_L	316 ± 4	320 ± 5	15.5 ± 0.8
HE8_L	571 ± 5	584 ± 8	10.0 ± 0.5

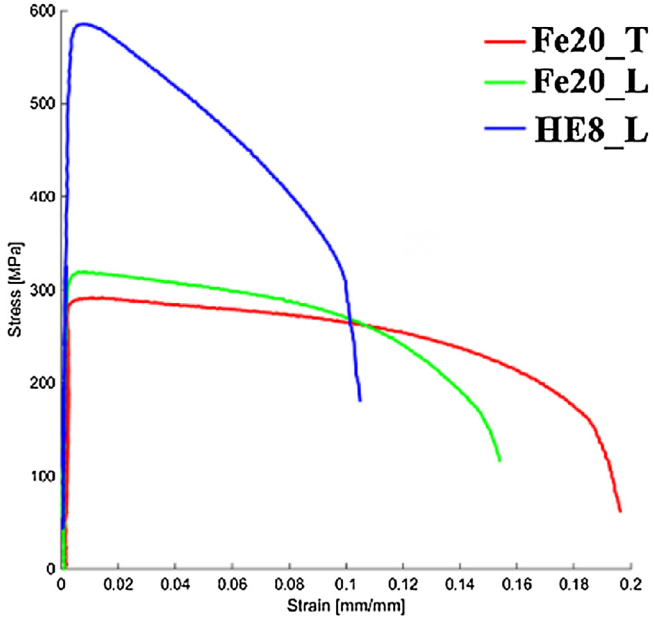

Fig. 11 – Exemplary stress–strain curves for tensile test.

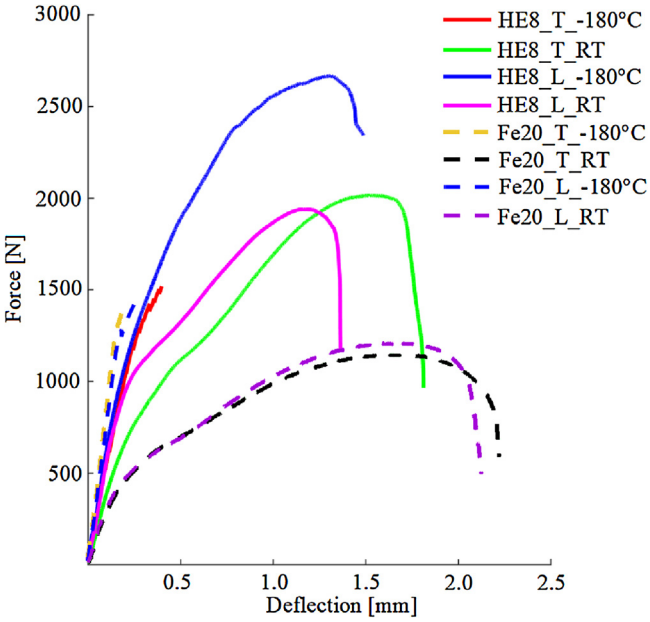

Fig. 12 – Exemplary force–deflection curves for mini-discs.

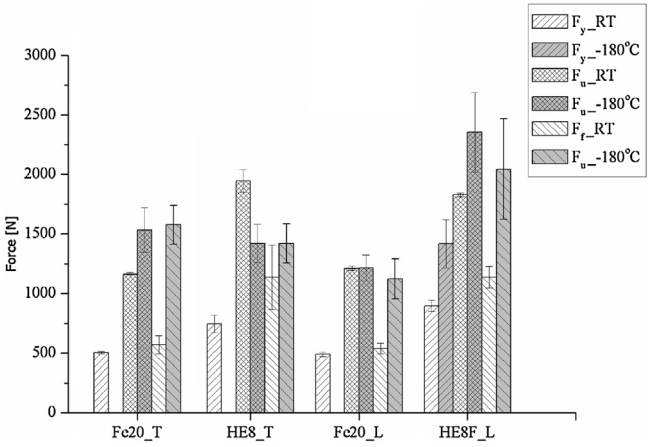

Fig. 13 – Force (yield, ultimate and failure) obtained for disc specimens deformed at room temperature and −180 °C.

specimens cut off from both the L and T cross-sections. The forces and deflections registered for the longitudinal and transverse cross-sections of the Fe20 rod did not exhibit significant differences.

The decrease in deflection and the increase in F_y, F_u and F_f observed for the UFG in comparison with the MC specimens were the result of strain hardening of the material. For the UFG iron, the ultimate and failure deflections registered for the HE8_T was 30% higher than those measured for the HE8F_L. For the UFG iron, the forces registered for different directions were similar.

At low temperature, the specimens Fe20_T, Fe20_L, HE8_T exhibited similar values of F_u and F_f. No yielding force or deflection was estimated. The deflection for the maximum force (U_u) was at a very low level. In the force–deflection curve, the third zone (membrane stretching) was not registered, which is typical for cleavage fracture. In comparison to the RT

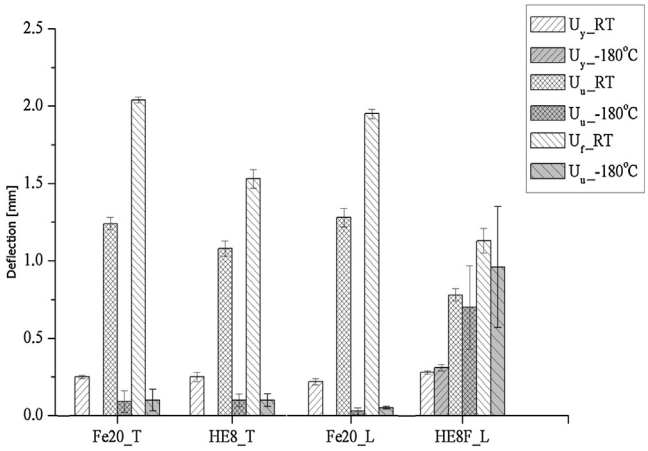

Fig. 14 – Deflection (yield, ultimate and failure) obtained for disc specimens deformed at room temperature and −180 °C.

the HE8_T specimens, obtained a lower strength than at the −180 °C. In the low temperature the HE8_L specimens, deformed similarly to the specimens damaged at RT. The material underwent plastification, the deflections U_y, U_u and U_f were at similar levels at both −180 °C and RT. The yield and ultimate force was over 40% higher at low temperature.

Figs. 15–17 present fracture surfaces for the disc specimens. For all the specimens loaded at RT, ductile behaviour was observed. On the bottom side of the specimens, there was a ''cap'' fracture resulting from the propagation of a circumferential crack. While SPT deformation the necking of specimens occurs near the contact area of the punch and investigated surface. All the fracture surfaces show microvoids and dimples (marked by arrows). For the MC material, the dimples were deeper and larger than those revealed for UFG. At low temperature, the character of the fractures was different, and depended on material and the direction of crack propagation path.

Both MC specimens show cleavage fractures. A crack was initiated in the middle of the discs and propagated radially. Fig. 15d and f shows the plain ''river'' facets typical of a brittle fracture. Between single facets brittle steps of the size from 40 to 80 μm were also observed (Fig. 15d). Additionally, secondary cracks were observed at low temperatures (Fig. 15e). Surface below the puncher did not undergo any plastic deformation. Cleavage fracture surface corresponds with very limited elongation on stress–strain curves.

In the HE8_T, the crack initiated in the centre of the disc and then propagated radially (similarly to the Fe20). Detailed studies revealed that the HE8_T discs damaged at low

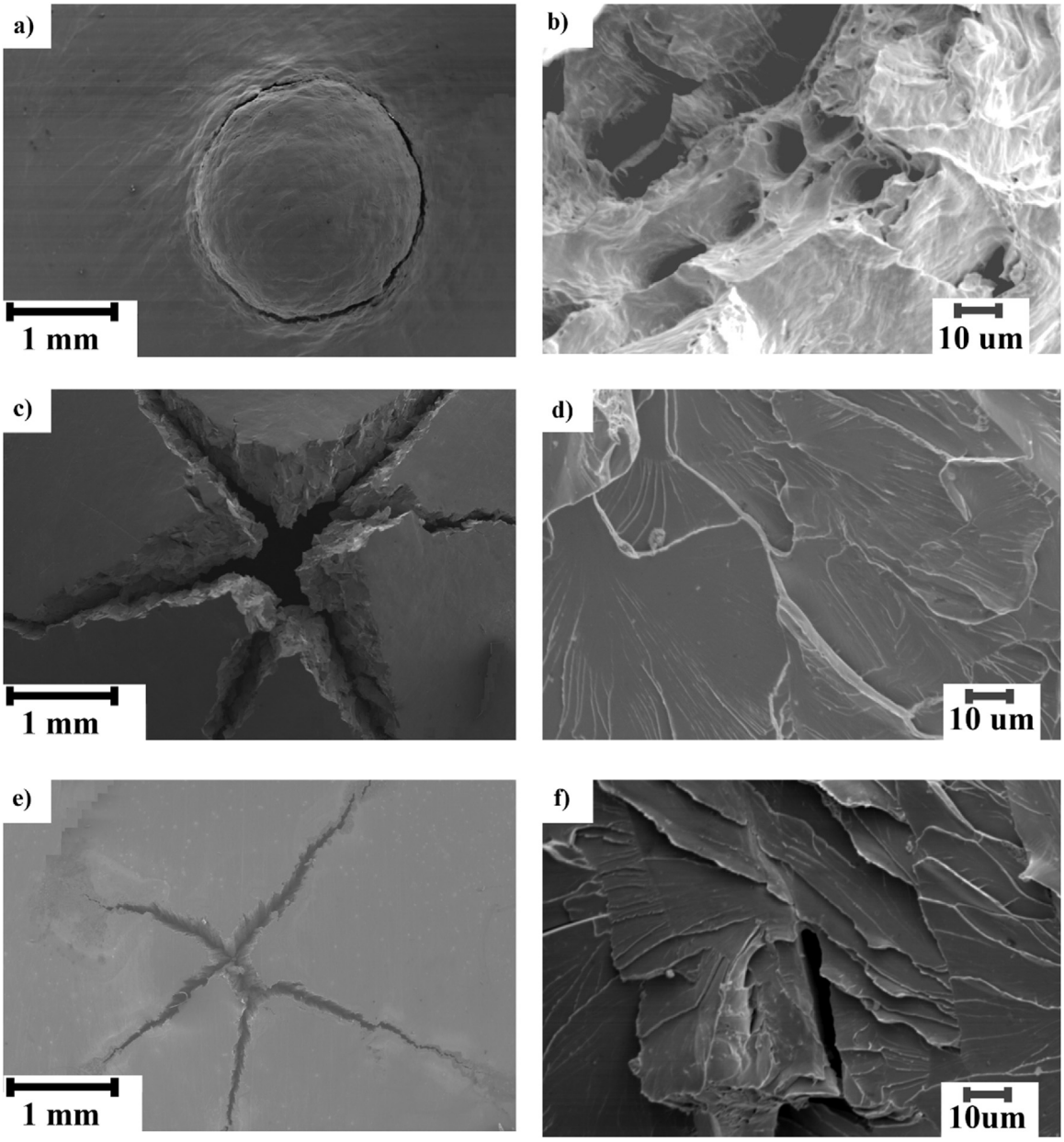

Fig. 15 – Fracture surface of (a and b) Fe20_T at RT; (c and d) Fe20_T at −180 °C; (e and f) Fe20_L at −180 °C.

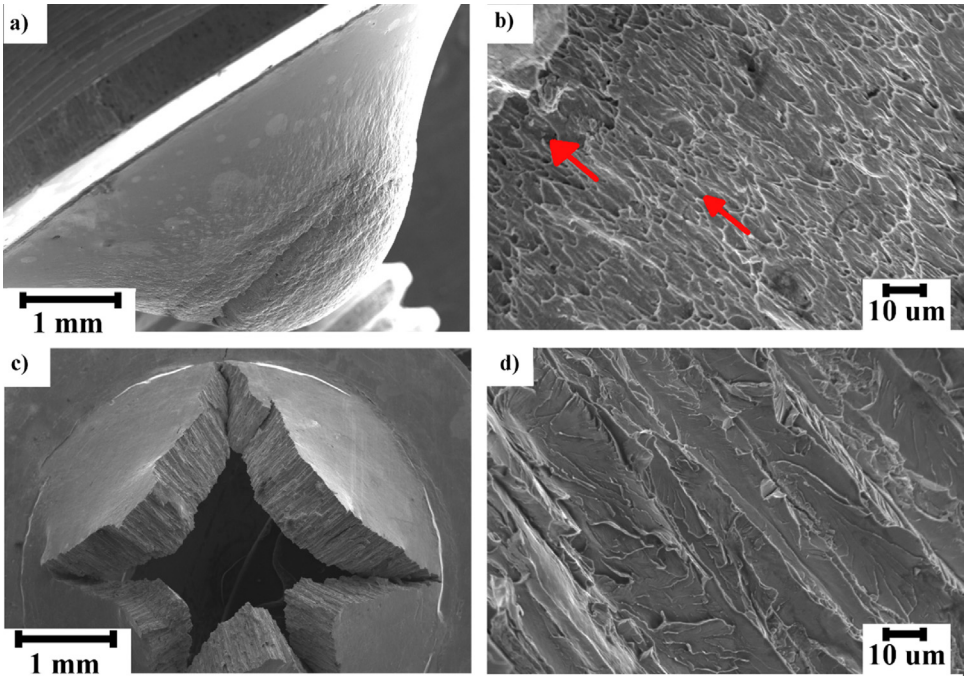

Fig. 16 – Fracture surface of HE8_T (a and b) at RT; (c and d) at −180 °C.

temperature had intercrystalline fracture surfaces. The facets parallel to the elongated grains, the direction of the force and the thickness of the specimens were observed. The distance between facets was from 10 to 20 μm, which was smaller than for Fe20 because of decrease in grain size. No single dimples was observed. Similarly to Fe20 brittle fracture promote fast crack propagation without plastification in macro observation and corresponds with force–deflection curves.

Comparison HE8F_L and HE8_T at room temperature shown that on longitudinal direction smaller amount of dipper and bigger dimples was observed, while on HE8_T many small and flat was revealed. The HE8F_L specimens loaded at low temperatures kept their plasticity (Fig. 17a). The fracture surface varied, depending on the crack propagation path. The plastic deformation caused by the puncher was visible in all of the specimens (Fig. 17a). Cracks propagated in two modes: intercrystalline (Fig. 17f) and transcrystalline (Fig. 17e). Some specimens fractured only in one mode, but most fractured in a mixed mode (Fig. 17c). The fracture path in mixed mode specimens was deflected from circumferential and transcrystalline to intergranular and straight. This caused the force drop in force–deflection curve. The intercrystalline facets observed on the fracture surface were parallel to the elongated grains but perpendicular to the applied force and specimen thickness. The facets look the same as those obtained for HE8_T. In the transcrystalline fracture, some delamination was revealed (Fig. 17e). On the middle part of the surface single dimples were observed (marked as arrows in Fig. 17e), while on the bottom where the elongation of grains in the highest the amount of dimples increased (marked as arrows in Fig. 17d). Fig. 18 shows exemplary force–deflection curves for the HE8F_L specimens obtained at low temperature force–deflection curve strongly depends on the fracturing mode. Specimens with the intercrystalline mode of fracture surface (blue curve) fractured at a very low force and deflection value, while those which damaged in the transcrystalline mode (red curve) proved to have good plasticity and high strength. For the specimens fractured in the mixed mode (green curve) a drop in force–deflection curve was observed.

3.2. *Mini-beam specimens*

Mini-beam specimens were prepared for a detailed investigation of the influence of microstructure anisotropy on fracture mode. The specimens were deformed by means of a tubular puncher, while the other parameters were the same as for the discs. The mini-beams were designed to force the direction of crack propagation. They were 2 mm in width, 0.8 mm in thickness, and 8 mm in length. For each direction 3–5 specimens were prepared. The specimens were cut off from the rods in three directions such that the axis of grain elongation was parallel or perpendicular to the axis of the mini-beam.

Figs. 19 and 20 show the results obtained from Fe20 mini-beams deformed by means of SPT.

The mini-beams of microcrystalline iron revealed similar average forces and deflections at both temperatures. Force–deflection curves of mini-beams Fe20 are presented in Fig. 21. All of the specimens deformed at room temperature exhibited 4 zones, while during loading at −180 °C no third zone was observed. This means that it was not possible to estimate yielding force and deflection. Specimens were damaged in elastic region, without plastic deformation. After reaching maximum force fracture occurred without any necking which is typical for brittle fracture. All Fe20 beams showed similar behaviour: similar ultimate force for room and −180 °C, high value of deflection at RT and negligible

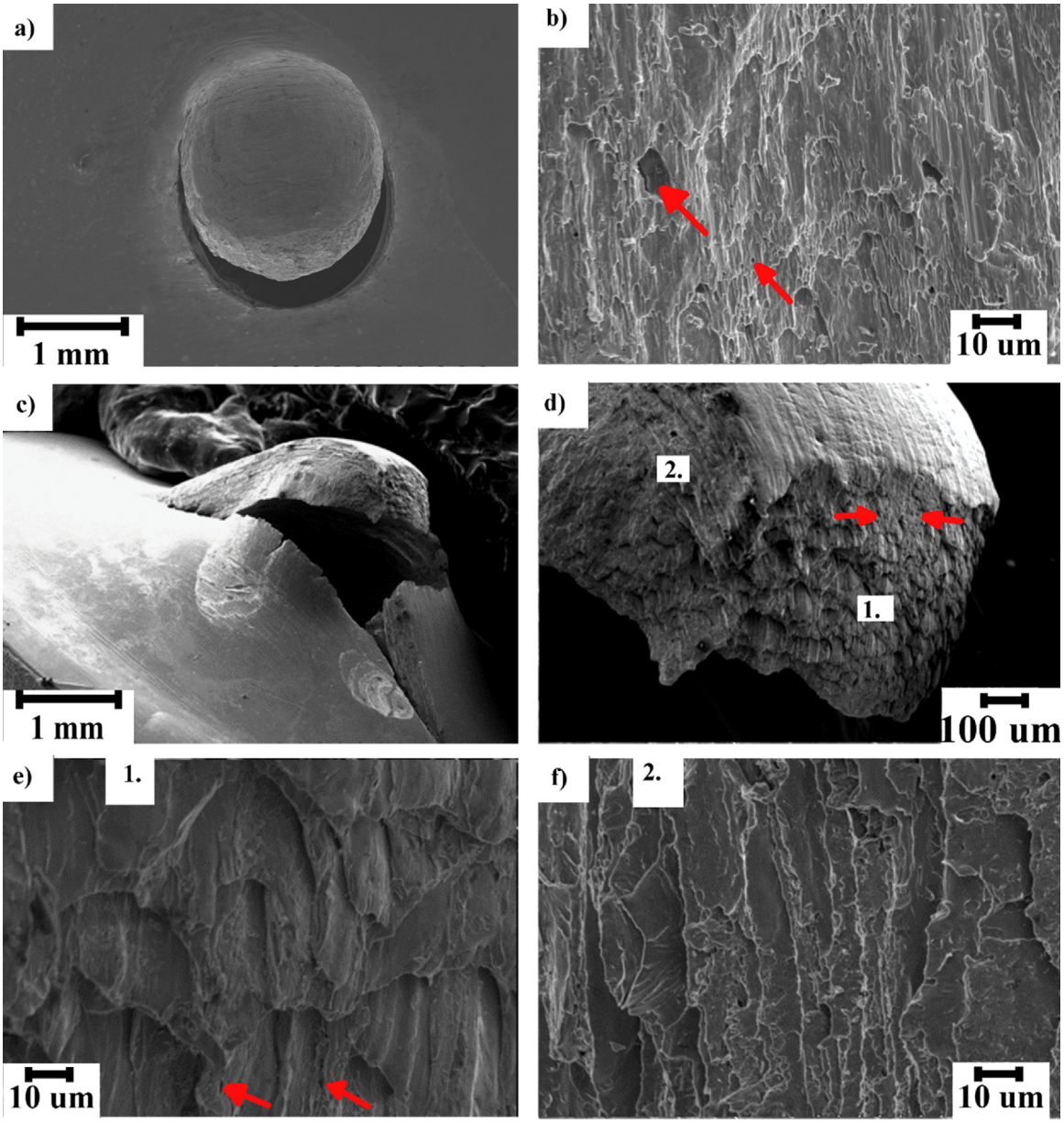

Fig. 17 – Fracture surface of HE8_L (a and b) at RT, (c–f) at −180 °C; (e) magnified area 1 and (f) magnified area 2 from (d).

deflection at −180 °C. The threshold of deflection was expected for microcrystalline iron because tests were carried out at temperature much lower then typical for DBTT of carbon steel [7]. No significant effect of specimen's anisotropy of MC iron on the SPT results was observed – specimens T1, L1, T2 obtained comparable results of force and deflection at both RT and −180 °C.

Observations of the fracture surface of the Fe20 mini-beams observed after SPT at −180 °C are presented in Fig. 22. The specimens deformed at RT were not fractured during loading – there were only some cracks on the bottom surface of the specimens. It was due to high plasticity of the Fe20 mini-beams at room temperature. The stand geometry did not allowed to carry out the test with higher deflection value. In general the fracture surface of all specimens were similar. All the specimens observed after SPT at −180 °C exhibited brittle fracture. Plane ''river'' facets were observed during SEM analysis. Even below the puncher no ductile effects were revealed. In the specimens cut off from the longitudinal direction, secondary cracks oriented perpendicularly to the applied force were observed (Fig. 22d and f, marked by arrows). For specimens cut off from another directions only the size of steps and ''river'' facets were different. For T1 and T2 specimens the elongated facets were revealed while for L1 elongation effect was not observed, which corresponds with the material microstructure.

Fig. 23 presents force–deflection curves registered for the UFG mini-beams. Figs. 24 and 25 show the average results obtained for the SPT mini-beams. For the ultrafine-grained

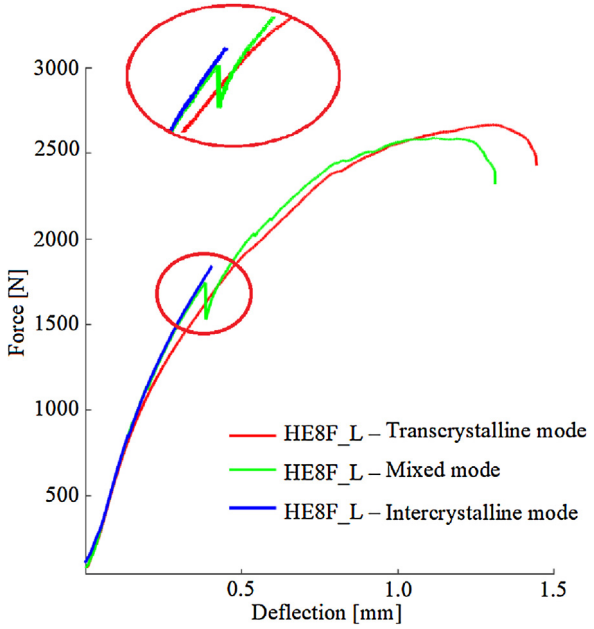

Fig. 18 – Force–deflection curves obtained for HE8F_L specimens deformed at −180 °C.

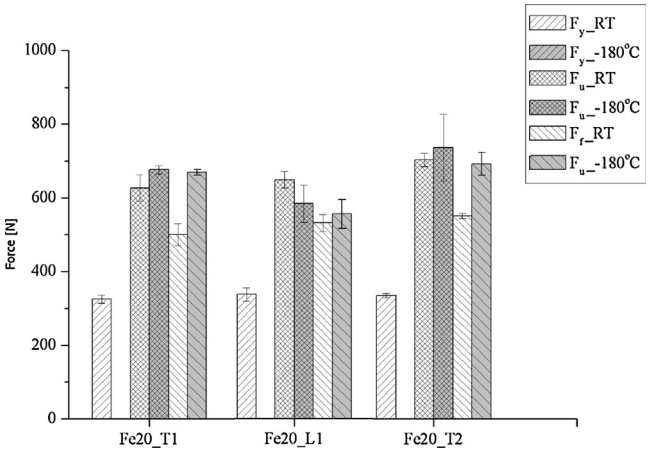

Fig. 19 – Force (yield, ultimate and failure) obtained for mini-beams Fe20 deformed at room temperature and −180 °C.

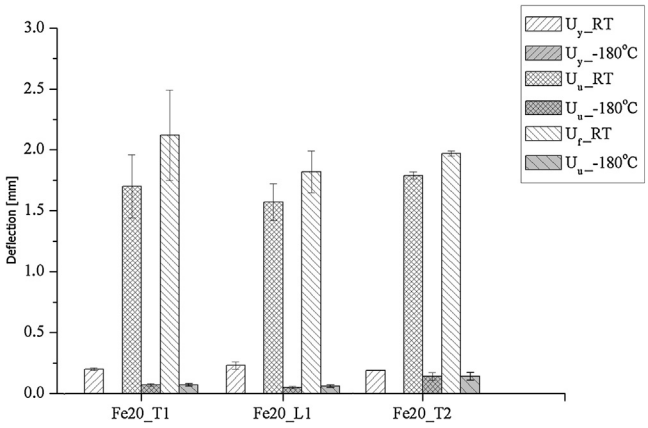

Fig. 20 – Deflection (yield, ultimate and failure) obtained for Fe20 mini-beams deformed at room temperature and −180 °C.

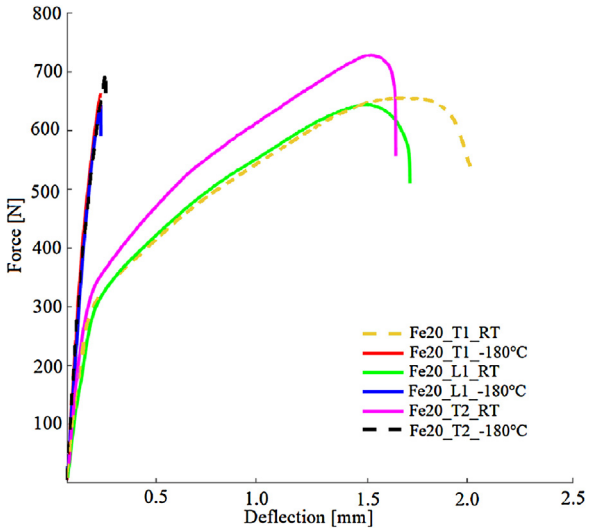

Fig. 21 – Exemplary force–deflection curves obtained for microcrystalline mini-beams.

iron deformed at RT, all of the specimens had a similar value of yield, ultimate and break force. The comparison of ultimate deflection showed no significant difference between the directions at room temperature. The highest deflection to failure was exhibited by the HE8F_T1 specimens, and this result was similar to those obtained for the disc specimens and mini-beams Fe20. It corresponds with the elongation of grains on the cross-section of specimens.

At low temperatures, the T1 and T2 mini-beams deformed in the same way. Similar values of forces and deflections were registered for those specimens. All of the specimens exhibited an increase in ultimate and break forces, and a decrease in deflection in comparison to RT. Only the L1 specimens maintained their ductility.

During the fracture surface observations, it was revealed that all of the specimens deformed at RT exhibit ductile fracture. Because of fine-grained structure small dimples and micro-voids were observed on the fracture surface. Near the edges of the specimens, some necking was observed (Fig. 26a). While macro observation it was observed that crack had propagated circumferentially which was similar to the mini-discs. On the bottom part the "cap" deformation of high radius was observed. Specimens T1 and T2 had a similar fracture surface at RT and −180 °C.

The cracks of HE8F_T1 and HE8F_T2 after SPT at low temperature exhibit plain facets (Fig. 26c and d), with some steps between the grains, suggesting brittle and intercrystalline fracture similar to that of the HE8_T disc specimens fracture. The steps were smaller than those for Fe20 which corresponds with fine-grained microstructure. No dimples on the fracture surface of the specimens were observed. While

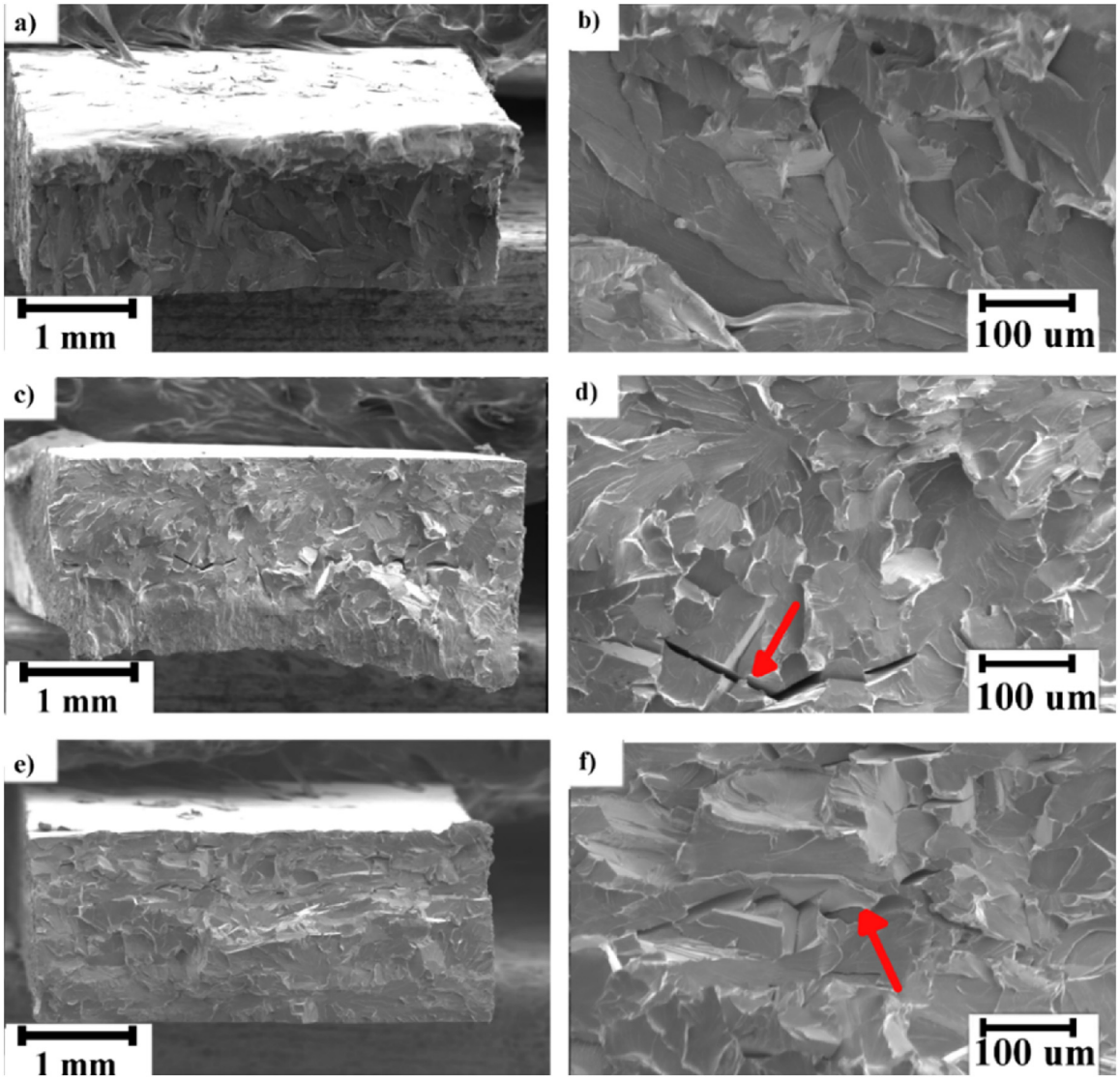

Fig. 22 – Fracture surface of Fe20 mini-beams deformed at −180 °C: (a and b) Fe20_T1_-180 °C; (c and d) Fe20_ L1_-180 °C; (e and f) Fe20_T2_-180 °C.

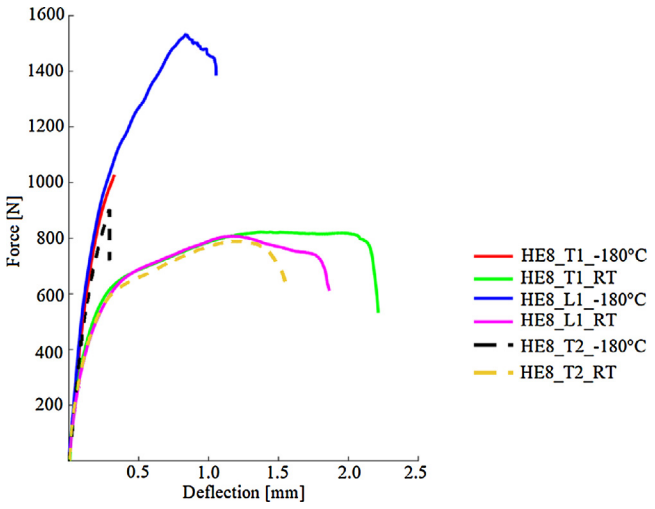

Fig. 23 – Exemplary force–deflection curves obtained for ultrafine-grained iron mini-beams.

macro observation necking and plastic deformation below the puncher had not been revealed. Specimens were fractured proportionally at all width in three pieces: two parts which were climbed between bottom and upper die and one between diameter of the tubular puncher.

The mini-beams cut off from the longitudinal direction exhibited a ductile fracture surface at RT and −180 °C. The HE8F_L1 specimens deformed at low temperature exhibited necking (Fig. 27c) and circumferential crack path with visible ''cap'' deformation in the bottom part of mini-beams. The specimens did not fracture into the pieces. On the fracture surface, dimples and micro-voids were observed, as in the case of the specimens deformed at RT (Fig. 27d). The specimens fractured in the transcrystalline mode. In macro observation specimens at RT and −180 °C looks similarly. But in higher resolution it might be seen that the size of dimples was bigger at RT which corresponds with higher ductility obtained at force–deflection curved. For −180 °C some quasi-brittle fracture and steps was observed while at RT only ductile element was revealed.

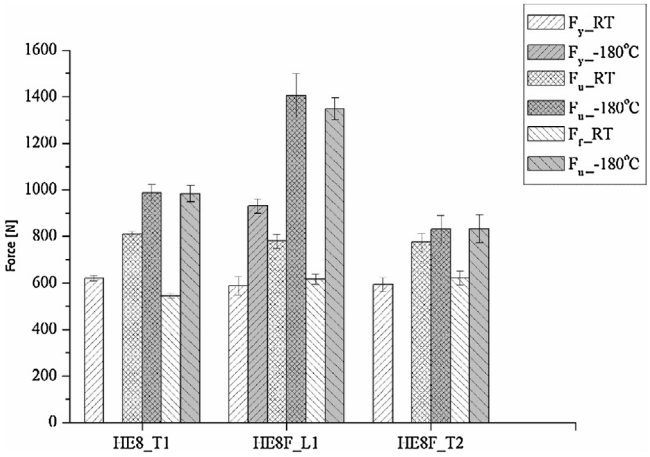

Fig. 24 – Force (yield, ultimate and failure) obtained for ultrafine-grained iron mini-beams deformed at room temperature and −180 °C.

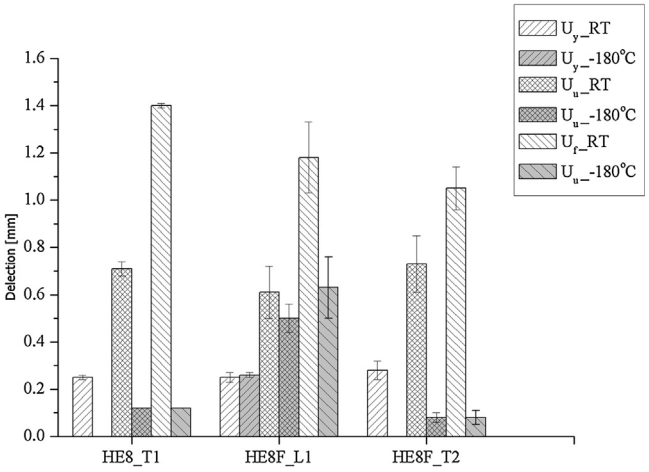

Fig. 25 – Deflection (yield, ultimate and failure) obtained for ultrafine-grained iron mini-beams deformed at room temperature and −180 °C.

Fig. 28 shows a schematic view of crack propagation in the UFG iron deformed by SPT at low temperature.

Comparison between the results obtained for MC and UFG iron showed higher force value for severely deformed material which was caused by grained refinement during hydrostatic extrusion, but it was with cost of ductility at RT. The research carried out on the mini-beams leads to the conclusion that transcrystalline fracture can be preserved at −180 °C only when the crack propagates crosswise to the axis of the elongated grains. When cracks propagate parallel to the axis of the elongated grains, the UFG iron fractured in the intercrystalline mode. Transcrystalline mode was observed for specimens were higher amount of grain boundaries had to be omitted during crack propagation. This specimen shows plastic behaviour even on low temperature. Based on Gizynski et al. research this can be concluded that in this direction the distance between dislocations were less than the critical one for ductile fracture. The transcrystalline fracture results in higher force and deflection to failure then intercrystalline. The effect of the crack propagation path on the mode of fracture and strength of UFG iron was also described by Leitner et al. for iron produced via HPT [20] and Hohenwarter et al. for iron produced via HPT [6] and ECAP [19]. Although they investigated iron produced by another SPD techniques, their results show similar relationship between fracture mode and crack propagation path. Leitner obtained the lowest roughness amplitude and fracture toughness value for the specimens were crack propagated parallel to the axis of the elongated grains. He claimed that it was due to very small distance on tipple points which the crack must deflect to propagate in the next grain boundary. This research was conducted at RT. At low temperature, Romelczyk et al. [5] and Gizynski et al. [2] obtained ductile fracture for iron produced by HE. Those work were carried out on specimens where the crack was propagated perpendicularly to the axis of the elongated grains, so no intercrystalline fracture was observed.

4. Summary

The anisotropy microstructure of UFG iron as a result of HE was revealed by mechanical and microstructural tests. The main method used to investigate the mechanical properties was the SPT technique. Two kinds of specimens (mini-discs and mini-beams) were used. Specimens were cut off from longitudinal and transverse cross-sections of iron rods. SPT was carried out at room temperature and −180 °C.

The main results of this research are:

- For UFG iron deformed at −180 °C crack path strongly depends on chosen specimen orientation. Fracture is intercrystalline only when a crack propagates parallel to the grain elongation axis. When a crack is oriented crosswise, a transcrystalline mechanism occurs.
- Plasticity of UFG iron at −180 °C also depends on specimen direction. For intercrystalline fracture no ductility was

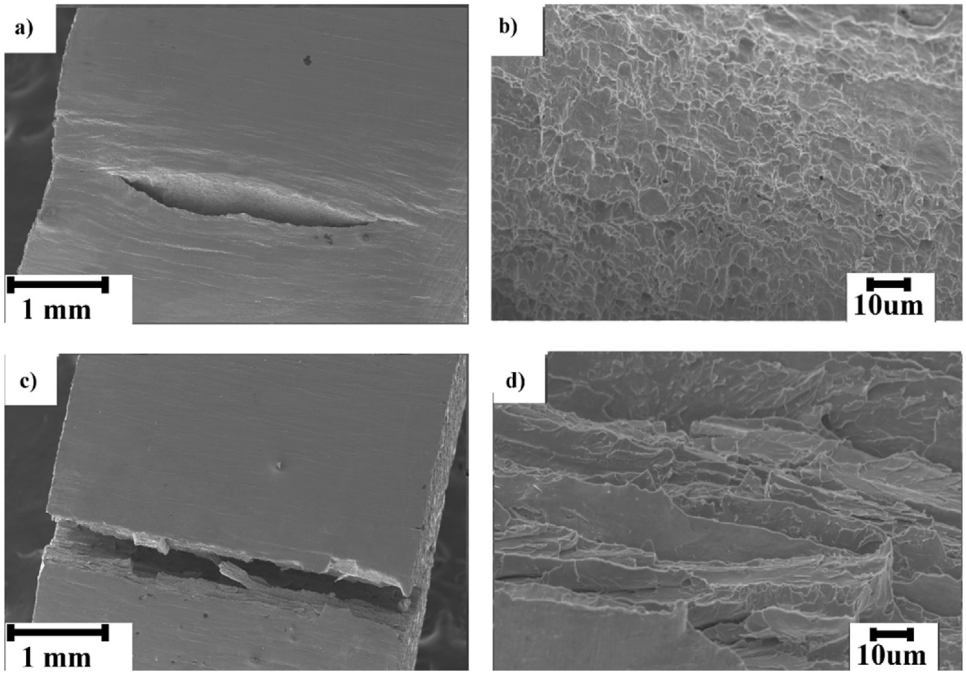

Fig. 26 – Fracture surface of HE8F_T2 (a and b) at RT, (c and d) at −180 °C.

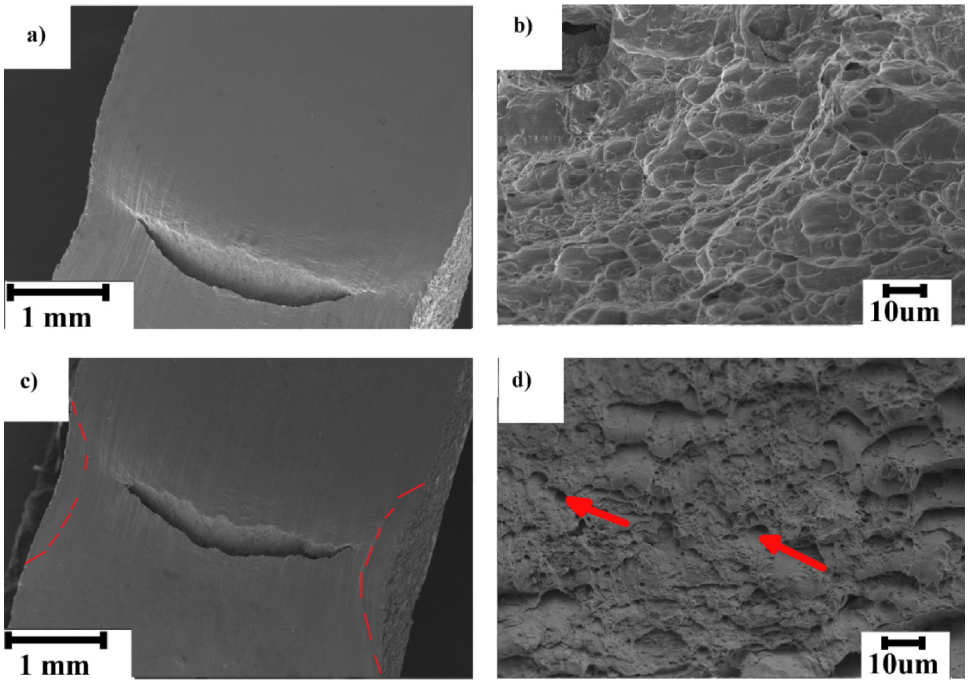

Fig. 27 – Fracture surface of HE8F_L1 (a and b) at RT, (c and d) at −180 °C.

observed on load–displacement curve. Specimens damaged in transcrystalline manner kept plasticity even at −180 °C.

- The microstructure anisotropy of UFG iron has a greater impact on fracture mode at low temperature than at room temperature.
- The MC iron did not exhibit noticeable effect of anisotropy on the SPT results.
- Mini-beams are an effective specimen shape for investigating the mechanical properties of materials available in small volumes. Mini-beams are also more useful than mini-discs for examining the anisotropy of materials.

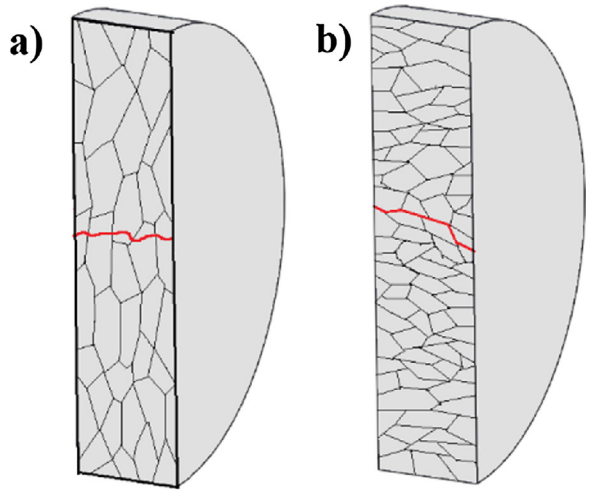

Fig. 28 – Comparison of fracture mode for (a) L1 and (b) T1 and T2 specimens.

Ethical statement

Authors state that the research was conducted according to ethical standards

Funding body

Polish National Science Centre, Contract No. UMO-2014/15/N/ST8/03388, and European Fund for Regional Development, Contract No. POIG.01.03.01-00-015/08.

REFERENCES

[1] J. Skogsrud, C. Thaulow, Effect of crystallographic orientation on nanomechanical modelling of an iron single crystal cracked cantilever beam, Mater. Sci. Eng. A 685 (2017) 274–283. http://dx.doi.org/10.1016/j.msea.2016.12.060.

[2] M. Gizynski, Z. Pakiela, W. Chrominski, M. Kulczyk, The low temperature fracture behaviour of hydrostatically extruded ultra-fine grained Armco iron, Mater. Sci. Eng. A 632 (2015) 35–42. http://dx.doi.org/10.1016/j.msea.2015.02.066.

[3] N.B. Shaw, G.M. Spink, The effect of temperature, specimen size, and geometry on the fracture toughness of a 3 pct NiCrMoV low pressure turbine disc steel, Metall. Trans. A 14 (1983) 751–759. http://dx.doi.org/10.1007/BF02643792.

[4] B. Tanguy, J. Besson, R. Piques, A. Pineau, Ductile to brittle transition of an A508 steel characterized by Charpy impact test, Part I: experimental results, Eng. Fract. Mech. 72 (2007) 49–72.

[5] B. Romelczyk, M. Kulczyk, Z. Pakieła, Microstructure and mechanical properties of fine-grained iron processed by hydroextrusion, Arch. Metall. Mater. 57 (2012) 1–5. http://dx.doi.org/10.2478/v10172-012-0098-0.

[6] A. Hohenwarter, R. Pippan, Anisotropic fracture behavior of ultrafine-grained iron, Mater. Sci. Eng. A 527 (2010) 2649–2656. http://dx.doi.org/10.1016/j.msea.2009.12.033.

[7] X.N. Zhang, Y.D. Qu, R. De Li, Low temperature impact toughness and fracture analysis of EN-GJS-400-18-LT ductile iron under instrumented impact load, J. Iron Steel Res. Int. 22 (2015) 864–869. http://dx.doi.org/10.1016/S1006-706X(15)30082-0.

[8] A. Hohenwarter, C. Kammerhofer, R. Pippan, The ductile to brittle transition of ultrafine-grained Armco iron: an experimental study, J. Mater. Sci. 45 (2010) 4805–4812. http://dx.doi.org/10.1007/s10853-010-4635-9.

[9] T.G. Langdon, Twenty-five years of ultrafine-grained materials: achieving exceptional properties through grain refinement, Acta Mater. 61 (2013) 7035–7059. http://dx.doi.org/10.1016/j.actamat.2013.08.018.

[10] P. Bazarnik, B. Romelczyk, Y. Huang, M. Lewandowska, T.G. Langdon, Effect of applied pressure on microstructure development and homogeneity in an aluminium alloy processed by high-pressure torsion, J. Alloys Compd. 688 (2016) 736–745. http://dx.doi.org/10.1016/j.jallcom.2016.07.149.

[11] P. Bazarnik, B. Romelczyk, M. Kulczyk, M. Lewandowska, The strength and ductility of 5483 aluminium alloy processed by various SPD methods, Mater. Sci. Forum 765 (2013) 423–428. http://dx.doi.org/10.4028/www.scientific.net/MSF.765.423.

[12] Y. Saito, N. Tsuji, H. Utsunomiya, T. Sakai, R. Hong, Ultra-fine grained bulk aluminum produced by accumulative roll-bonding proces, Scr. Mater. 40 (1999) 795–800.

[13] A.P. Zhilyaev, T.G. Langdon, Using high-pressure torsion for metal processing: fundamentals and applications, Prog. Mater. Sci. 53 (2008) 893–979. http://dx.doi.org/10.1016/j.pmatsci.2008.03.002.

[14] Y.T. Zhu, T.G. Langdon, Influence of grain size on deformation mechanisms: an extension to nanocrystalline materials, Mater. Sci. Eng. A 409 (2005) 234–242. http://dx.doi.org/10.1016/j.msea.2005.05.111.

[15] Z.Y.Y. Wang, E. Ma, R.Z. Valiev, Tough nanostructured metals at cryogenic temperatures, Adv. Mater. 16 (2004) 328–331.

[16] J.R. Rice, Dislocation nucleation from a crack tip: an analysis based on the Peierls concept, J. Mech. Phys. Solids 40 (1992) 239–271. http://dx.doi.org/10.1016/S0022-5096(05)80012-2.

[17] I.A. Ovid'ko, A.G. Sheinerman, Ductile vs. brittle behavior of pre-cracked nanocrystalline and ultrafine-grained materials, Acta Mater. 58 (2010) 5286–5294. http://dx.doi.org/10.1016/j.actamat.2010.05.058.

[18] R.W. Armstrong, S.D. Antolovich, The grain size dependence of cleavage cracking in α-iron, in: Proc. 18th Eur. Conf. Fract., 2010.

[19] A. Hohenwarter, R. Pippan, Fracture of ECAP-deformed iron and the role of extrinsic toughening mechanisms, Acta Mater. 61 (2013) 2973–2983. http://dx.doi.org/10.1016/j.actamat.2013.01.057.

[20] T. Leitner, A. Hohenwarter, W. Ochensberger, R. Pippan, Fatigue crack growth anisotropy in ultrafine-grained iron, Acta Mater. 126 (2017) 154–165. http://dx.doi.org/10.1016/j.actamat.2016.12.059.

[21] T. Wejrzanowski, W. Spychalski, K. Różniatowski, K. Kurzydłowski, Image based analysis of complex microstructures of engineering materials, Int. J. Appl. Math. Comput. Sci. 18 (2008) 33–39. http://dx.doi.org/10.2478/v10006-008-0003-1.

[22] R.M. Molak, K. Paradowski, T. Brynk, L. Ciupinski, Z. Pakiela, K.J. Kurzydlowski, Measurement of mechanical properties in a 316L stainless steel welded joint, Int. J. Press. Vessel. Pip. 86 (2009) 43–47. http://dx.doi.org/10.1016/J.IJPVP.2008.11.002.

[23] M.P. Manahan, A.S. Argon, O.K. Harling, The development of a miniaturized disk bend test for the determination of postirradiation mechanical properties, J. Nucl. Mater. 104 (1981) 1545–1550. http://dx.doi.org/10.1016/0022-3115(82)90820-0.

[24] B. Romelczyk, T. Brynk, R.M. Molak, A. Jastrzębska, K. Nowak, Z. Pakiela, Magnesium AZ91 alloy cast mechanical properties measured by the miniaturized disc-bend test, Key Eng. Mater. 592–593 (2013) 805–808. http://dx.doi.org/10.4028/www.scientific.net/KEM.592-593.805.

[25] R. Hurst, K. Matocha, Experiences with the European code of practice for small punch testing for creep, tensile and fracture behavior, in: ف Proc 3th Int. Conf. SSTT, 2014, 1–26, ص.

[26] F. Dobeš, K. Milička, Comparison of conventional and small punch creep tests of mechanically alloyed Al–C–O alloys, Mater. Charact. 59 (2008) 961–964. http://dx.doi.org/10.1016/j.matchar.2007.08.006.

[27] M. Abendroth, M. Kuna, Identification of ductile damage and fracture parameters from the small punch test using neural networks, Eng. Fract. Mech. 73 (2006) 710–725. http://dx.doi.org/10.1016/j.engfracmech.2005.10.007.

[28] E. Altstadt, M. Serrano, M. Houska, A. García-Junceda, Effect of anisotropic microstructure of a 12Cr-ODS steel on the fracture behaviour in the small punch test, Mater. Sci. Eng. A 654 (2016) 309–316. http://dx.doi.org/10.1016/j.msea.2015.12.055.

[29] R.M. Molak, M.E. Kartal, Z. Pakiela, K.J. Kurzydlowski, The effect of specimen size and surface conditions on the local mechanical properties of 14MoV6 ferritic–pearlitic steel, Mater. Sci. Eng. A 651 (2016) 810–821. http://dx.doi.org/10.1016/j.msea.2015.11.037.

[30] T.E. García, C. Rodríguez, F.J. Belzunce, C. Suárez, Estimation of the mechanical properties of metallic materials by means of the small punch test, J. Alloys Compd. 582 (2014) 708–717. http://dx.doi.org/10.1016/j.jallcom.2013.08.009.

[31] M.F.G.Q. Han, Z. Lee, S.R. Nutt, E.J. Lavernia, Mechanical properties of iron processed by severe plastic deformation, Metall. Mater. Trans. A 34 (2003) 71–83.